Article

Stable, high-performance sodium-based plasmonic devices in the near infrared

Yang Wang[1,7], Jianyu Yu[1,7], Yi-Fei Mao[2,7], Ji Chen[1,3,7], Suo Wang[2], Hua-Zhou Chen[2], Yi Zhang[4], Si-Yi Wang[2], Xinjie Chen[1], Tao Li[1,3], Lin Zhou[1,3✉], Ren-Min Ma[2,5✉], Shining Zhu[1✉], Wenshan Cai[6] & Jia Zhu[1✉]

Plasmonics enables the manipulation of light beyond the optical diffraction limit[1–4] and may therefore confer advantages in applications such as photonic devices[5–7], optical cloaking[8,9], biochemical sensing[10,11] and super-resolution imaging[12,13]. However, the essential field-confinement capability of plasmonic devices is always accompanied by a parasitic Ohmic loss, which severely reduces their performance. Therefore, plasmonic materials (those with collective oscillations of electrons) with a lower loss than noble metals have long been sought[14–16]. Here we present stable sodium-based plasmonic devices with state-of-the-art performance at near-infrared wavelengths. We fabricated high-quality sodium films with electron relaxation times as long as 0.42 picoseconds using a thermo-assisted spin-coating process. A direct-waveguide experiment shows that the propagation length of surface plasmon polaritons supported at the sodium–quartz interface can reach 200 micrometres at near-infrared wavelengths. We further demonstrate a room-temperature sodium-based plasmonic nanolaser with a lasing threshold of 140 kilowatts per square centimetre, lower than values previously reported for plasmonic nanolasers at near-infrared wavelengths. These sodium-based plasmonic devices show stable performance under ambient conditions over a period of several months after packaging with epoxy. These results indicate that the performance of plasmonic devices can be greatly improved beyond that of devices using noble metals, with implications for applications in plasmonics, nanophotonics and metamaterials.

Of the plasmonic materials, the noble metals, particularly silver and gold, are those most often used owing to their relatively low loss. However, the optical loss of the two metals is still not commercially acceptable and has been the primary limiting factor for the widespread applications of plasmonics[1–13]. Therefore, there has been a persistent search for low-loss alternatives[14–16], such as crystalline metals, intermetallic composites, metal alloys, nitrides and oxides.

Of these alternatives, the alkali metals, such as sodium, have long been regarded as ideal plasmonic materials[14–17], primarily because of their low intraband damping rate. When light interacts with a plasmonic metal, it suffers from scattering damping of the intraband transition of electrons (γ_p)[15], and the total intraband damping rate can be obtained by:

$$\gamma_p = \gamma_{e\text{-}p} + \gamma_{e\text{-}e} + \gamma_{e\text{-}i}, \tag{1}$$

where $\gamma_{e\text{-}p}$, $\gamma_{e\text{-}e}$ and $\gamma_{e\text{-}i}$ are the optical damping rates that originate from electron–phonon scattering, electron–electron scattering and electron–impurity scattering, respectively. The overall intraband

optical loss γ_p of sodium is estimated to be around 0.010 eV (Supplementary Information), corresponding to a relaxation time of 0.42 ps. For comparison, silver has an intraband optical loss of 0.021 eV and a relaxation time of 0.20 ps, based on the Drude–Lorentz model[18]. In addition, sodium has electron gases with a density of 2.65×10^{22} cm^{-3} (ref. [17]), which is approximately half that of silver, which is another important factor contributing to a decreased optical loss.

Although sodium has been predicted to be an ideal plasmonic material for years, the experimental exploration of sodium as a plasmonic material has been limited, apart from the early measurement of its optical constants[19,20] and the demonstration of localized plasmon resonances in alkali metal nanoparticles precipitated within crystal matrices[21]. Because of its high chemical reactivity, fabricating sodium-based structures using conventional metal-deposition techniques, such as physical deposition, has been challenging[19].

Here, by taking advantage of the low melting point of sodium, we have developed a thermo-assisted spin-coating process for fabricating a sodium film, as shown in Fig. 1a (optical images of the procedure in Extended Data Fig. 1a). The sodium metal is heated up to 160 °C to

[1]National Laboratory of Solid State Microstructures, Collaborative Innovation Center of Advanced Microstructures, Jiangsu Key Laboratory of Artificial Functional Materials, College of Engineering and Applied Sciences, Nanjing University, Nanjing, People's Republic of China. [2]State Key Lab for Mesoscopic Physics and School of Physics, Peking University, Beijing, People's Republic of China. [3]Key Laboratory of Intelligent Optical Sensing and Manipulation, Ministry of Education, Nanjing University, Nanjing, People's Republic of China. [4]School of Information and Electronic Engineering, Zhejiang Gongshang University, Hangzhou, People's Republic of China. [5]Frontier Science Center for Nano-optoelectronics and Collaborative Innovation Center of Quantum Matter, Peking University, Beijing, People's Republic of China. [6]School of Electrical and Computer Engineering, Georgia Institute of Technology, Atlanta, GA, USA. [7]These authors contributed equally: Yang Wang, Jianyu Yu, Yi-Fei Mao, Ji Chen. ✉e-mail: linzhou@nju.edu.cn; renminma@pku.edu.cn; zhusn@nju.edu.cn; jiazhu@nju.edu.cn
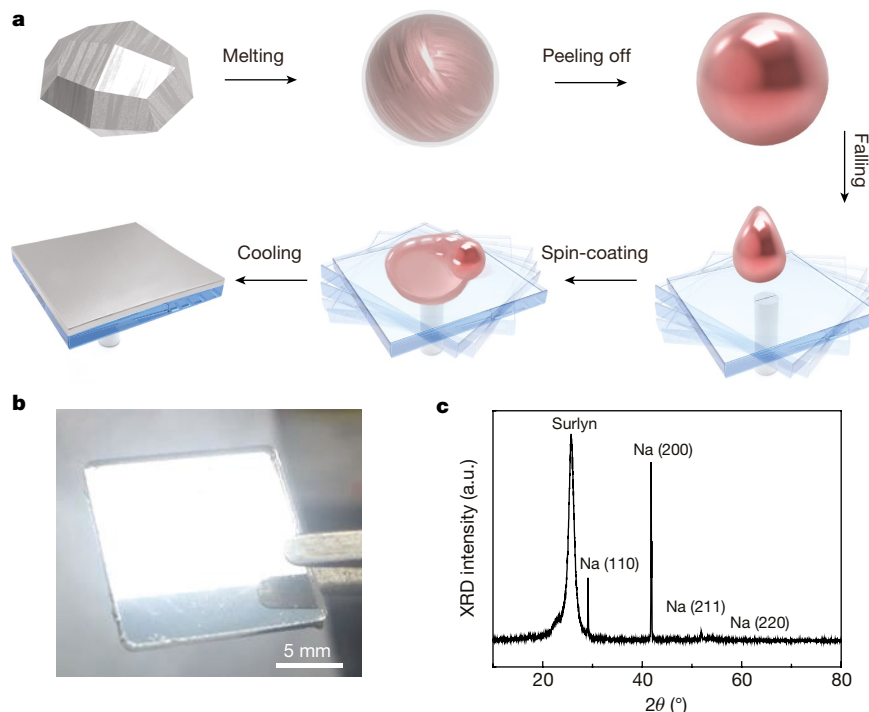
Fig. 1 | Sodium film fabricated by a thermo-assisted spin-coating process. a, Schematic of the process flow. A piece of sodium is heated and melted while inner impurities diffuse towards the surface during this thermal annealing process; the thin oxide shell incorporating the impurities covers the melted sodium droplet and is then peeled off; the cleaned sodium droplet is spin-coated onto a rotating quartz substrate; the sodium film then forms on the quartz surface with a smooth interface. **b**, Photograph of the spin-coated sodium film on quartz. Scale bar, 5 mm. **c**, X-ray diffraction pattern of the spin-coated sodium film. The sodium film is covered with Surlyn as packaging. XRD, X-ray diffraction; a.u., arbitrary units.

form a droplet. During this thermal annealing process, impurities diffuse towards the surface, which can then be peeled off to purify the sodium droplet. The purified sodium droplet, which has a luminous appearance, is then spin-coated onto an ultrasmooth quartz substrate (roughness of about 0.1 nm; Extended Data Fig. 1b). Once the sodium droplet touches the surface of spinning quartz, an ultrasmooth sodium film forms (Fig. 1b) owing to the strong centrifugal forces of the rotating quartz and fast solidification. The entire process is conducted inside a glove box with an inert atmosphere. The X-ray diffraction pattern shows that the sodium film produced is polycrystalline (Fig. 1c, where the sample is sealed with Surlyn, an ionomer resin transparent to X-rays for a wide range of angles).

To evaluate the optical properties of the prepared sodium film, we measured its dielectric function in the wavelength range 400–1,500 nm using a spectroscopic ellipsometer. Figure 2a depicts the measured dielectric functions versus wavelength of the sodium film (solid circle symbols), which exhibits a lower optical loss than reported values for silver over a wide range of wavelengths (see Extended Data Fig. 2 for comparison).

To quantitatively analyse the loss mechanisms of the sodium film, we used a Drude–Lorentz model[16,22] to fit the measured dielectric curves (dashed lines in Fig. 2a), which is expressed as:

$$\varepsilon(\omega) = \varepsilon_b - \omega_p^2/(\omega^2 + i\omega\gamma_p) + f_1\omega_1^2/(\omega_1^2 - \omega^2 - i\omega\gamma_1), \qquad (2)$$

where ε_b is the polarization response from the core electrons (background permittivity), ω_p is the bulk plasma frequency, γ_p is the Drude damping rate, f_1 and ω_1 are the amplitude and resonant frequency of the inter-band transition, respectively, and γ_1 is the related interband damping rate. The fitting parameters for the sodium film are $\varepsilon_b = 0.500$, $\omega_p = 5.414$ eV, $\omega_1 = 2.945$ eV, $f_1 = 0.280$, $\gamma_1 = 2.706$ eV and $\gamma_p = 0.010$ eV. The relaxation time τ can be determined by the Drude damping rate, which is 0.42 ps. Notably, compared to the bulk silver materials, the optical damping rate of our sodium film is reduced by half and the relaxation time is doubled. ($\gamma_p = 0.021$ eV and $\tau = 0.20$ ps for silver[18]).

To further illustrate the reduced optical loss of our sodium film compared to silver, we calculated the figure of merit (defined by $-\varepsilon_1/\varepsilon_2$; ref. [16]), as shown in Fig. 2b. We chose two sets of silver data from recent publications for comparison[23,24]. It can clearly be seen that our sodium film has state-of-the-art performance in the near-infrared region of the spectrum.

This low-loss sodium film provides an opportunity to improve the performance of plasmonic devices. We now demonstrate high-performance sodium-based plasmonic waveguides and plasmonic nanolasers at near-infrared wavelengths. A two-step fabrication process—spin-coating of sodium and packaging—was conducted inside a glove box. All characterizations were carried out under ambient conditions, including the measurements of the dielectric function, plasmonic waveguiding and plasmonic lasing.

Figure 2c shows the schematics of the sodium-based plasmonic waveguide structure. The left coupler converts the incident laser beam to surface plasmon polaritons (SPPs) (Fig. 2d, left light spot), which propagate along the sodium–quartz interface and then become coupled to free space via the right coupler (Fig. 2d, right light spot). The intensity of the SPPs decreases exponentially as a function of distance. Various propagation separations were measured to fit the intensity decay curve (Fig. 2e), to obtain the propagation lengths (δ_{SPP}) at different wavelengths on the sodium–quartz interface (Fig. 2f). The inset to Fig. 2e depicts the scanning electron microscopy (SEM) image of the launching and outcoupling structures for the SPP propagation measurements (the fabrication process for the plasmonic waveguide devices is described in Extended Data Fig. 3). It is clear that the sodium film supports a δ_{SPP} of 200 μm at a wavelength of 1,500 nm, which represents state-of-the-art performance for plasmonic waveguides (see Extended Data Fig. 4a–c for comparison with silver).

In addition to the propagation length, the effective mode size—expressed as the sum of the decay lengths (skin depths) in the dielectric
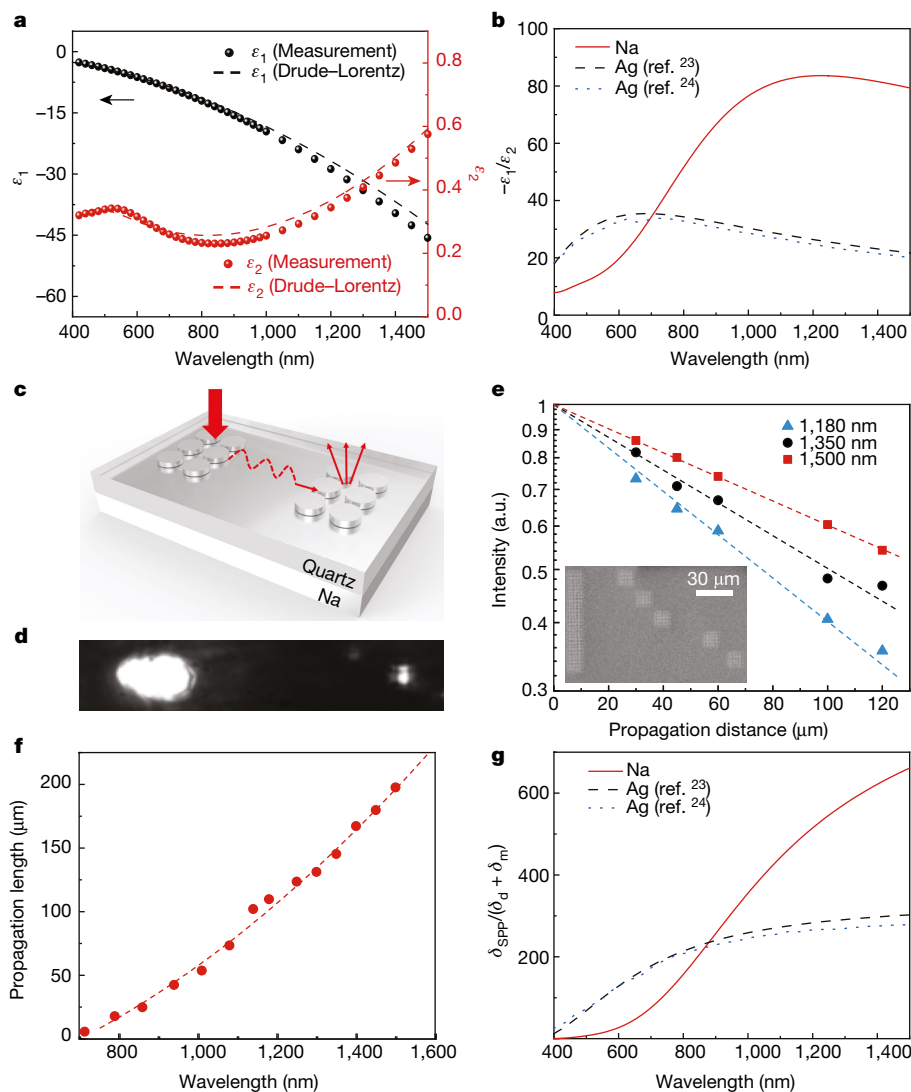
Fig. 2 | Dielectric functions of sodium film and sodium-based plasmonic waveguides. a, Real and imaginary parts of the dielectric functions ($\varepsilon = \varepsilon_1 + i\varepsilon_2$) of the sodium film (solid circles). Dashed lines show the Drude–Lorentz fittings. **b**, Figure of merit ($-\varepsilon_1/\varepsilon_2$) comparison for sodium (this work) and silver (from refs. [23,24]). Comparisons with various data for silver in the literature are shown in Extended Data Fig. 4. **c**, Schematic of a sodium-based plasmonic waveguiding structure with two nanostructured couplers. The coupling structures are pillar arrays. **d**, Optical image of the light spots of sodium-based plasmonic waveguiding. The distance between the launching and output structures is 100 µm. **e**, Propagation measurements at wavelengths of 1,180 nm, 1,350 nm and 1,500 nm for sodium, with exponential curves fitted to the data. Inset, SEM image of the launching and outcoupling structures without sodium coating. Scale bar, 30 µm. **f**, The fitted propagation length at different wavelengths on the sodium–quartz interface. The dashed line is a fit to the data. **g**, Figure of merit for plasmonic waveguides for sodium and silver, which is defined as the ratio of propagation length to skin depth $\delta_{SPP}/(\delta_d + \delta_m)$.

δ_d and in the metal δ_m—is another essential parameter of the plasmonic waveguide, characterizing the field-confinement capability. Therefore, we can define the figure of merit of the plasmonic waveguide as the ratio of the propagation length over skin depth $\delta_{SPP}/(\delta_d + \delta_m)$. The figures of merit of the plasmonic waveguide of sodium and silver are plotted in Fig. 2g, further identifying sodium as a promising material of choice for plasmonic-waveguide-based applications at the near-infrared wavelengths (see Extended Data Fig. 4d for comparison with more data for silver).

The plasmonic nanolaser is another widely studied plasmonic device for which a low-loss metal has long been sought in order to achieve a lower lasing threshold and power consumption[7,25–30]. We fabricated sodium-based plasmonic nanolasers based on a metal–insulator–semiconductor gap plasmonic mode configuration[31,32]. As shown in Fig. 3a, b, the device consists of an InGaAsP multi-quantum-wells (MQWs) nanodisk on top of sodium film with a 7-nm-thick Al$_2$O$_3$ layer in between (see Extended Data Fig. 5 for fabrication details). Figure 3c shows the SEM image of an InGaAsP MQWs nanodisk without the sodium coating, with diameter and thickness 1.2 µm and 200 nm, respectively. Figure 3d–f shows the simulated electric-field distributions of the lasing plasmonic mode obtained by three-dimensional full-wave simulations. The electric field is strongly confined at the interface between InGaAsP and sodium, thus exhibiting a pronounced plasmonic feature.

The sodium-based plasmonic nanolaser exhibits single-mode lasing with a low lasing threshold under optical pumping (Fig. 3g). Notably, pronounced resonance peaks appear in the spontaneous emission spectrum below the lasing threshold, which indicates the high quality factor Q of the sodium-based plasmonic nanocavity[31,32]. When we pump the device above the lasing threshold, a single lasing mode becomes dominant at 1,257 nm with a much narrower linewidth than spontaneous emission. The side-mode suppression ratio of this laser is about 20 dB (pump intensity 475 kW cm^{-2}; see Extended Data Fig. 6). We have identified this lasing cavity mode as the gap plasmonic whispering-gallery mode with an azimuthal order of $l = 15$ and a cold
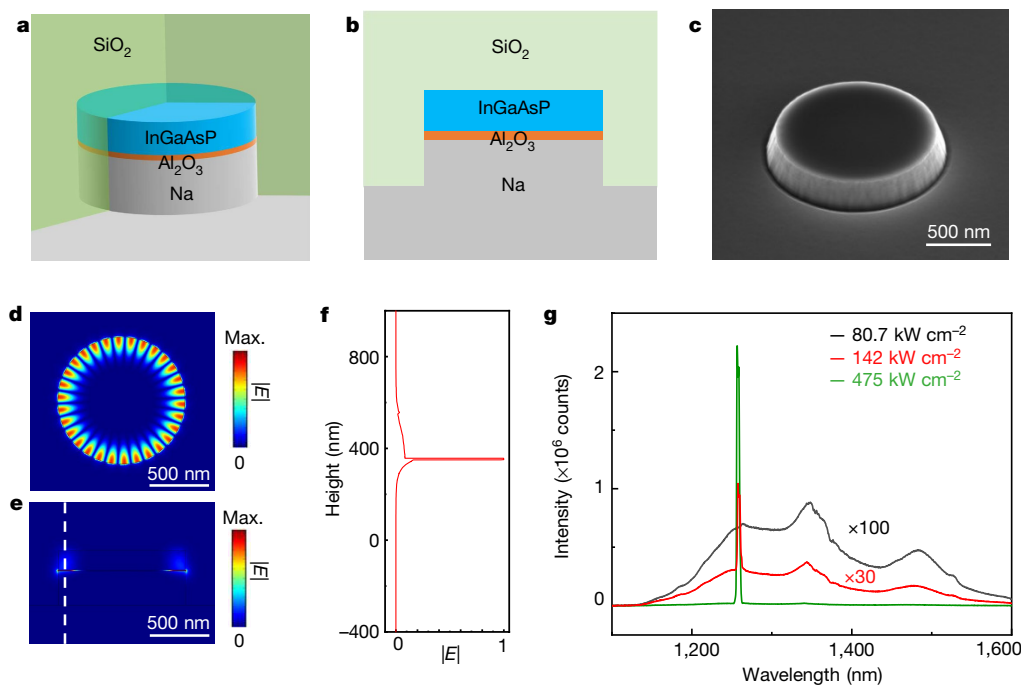
Fig. 3 | Room-temperature sodium-based plasmonic nanolaser. a, b, Schematics of a sodium-based plasmonic nanolaser in three dimensions (a) and two dimensions (b). c, SEM image of an InGaAsP MQWs nanodisk, without sodium coating. Scale bar, 500 nm. d, e, Top (d) and side (e) views of the electric-field distribution of the calculated lasing mode. The mode is a plasmonic whispering-galley mode where the field is strongly confined at the interface between the MQWs and sodium. f, Normalized electric-field profile along the white dashed line in e. g, Spectra of spontaneous emission (black), amplified spontaneous emission (red), and single-mode laser emission (green) of the sodium-based plasmonic nanolaser.

cavity quality factor of about 340 using full-wave simulation (see Extended Data Fig. 7).

The threshold of the laser can be extracted from the evolution of the normalized spectra of the device versus the pump power and the S-shaped light–light curve (Fig. 4a, b). The threshold of the sodium-based plasmonic nanolaser is about 140 kW cm^{-2}, which, to our knowledge, is the lowest reported value among near-infrared plasmonic nanolasers at room temperature (see Extended Data Table 1 and Extended Data Fig. 8).

Owing to the high material dispersion, plasmonic modes possess a higher group index than photonic modes. Here we reveal photonic-to-plasmonic mode jumping by tracking the group index of the lasing modes with decreased cavity diameter (Fig. 4c). In the experiment, we observe a sudden clear increase of the group index at a device diameter of about 2 µm, which indicates that plasmonic mode lasing becomes dominant for smaller cavities. To further demonstrate

the effect of sodium in lasing, we carried out a control experiment where bare InGaAsP MQWs nanodisks are optically pumped. However, for the devices with the same diameter as the one shown in Fig. 3, no lasing behaviour is observed till they are burned by the pump laser, which results from the larger radiation loss for the bare dielectric cavities[33].

One natural concern with regard to the use of sodium for plasmonic devices is its stability. It is therefore encouraging to find that these sodium-based plasmonic devices remain stable over a long period of time after the packaging of quartz and epoxy. More details of our extensive accelerated-ageing tests of sodium-based devices (high temperature and high air humidity) can be found in Extended Data Fig. 9. Our nanolaser devices remain functional at a low threshold even after six months (Extended Data Fig. 9g).

In summary, we have demonstrated a method of fabricating high-quality sodium films. Sodium-based plasmonic waveguides and nanolasers have been realized and their high performance is verified
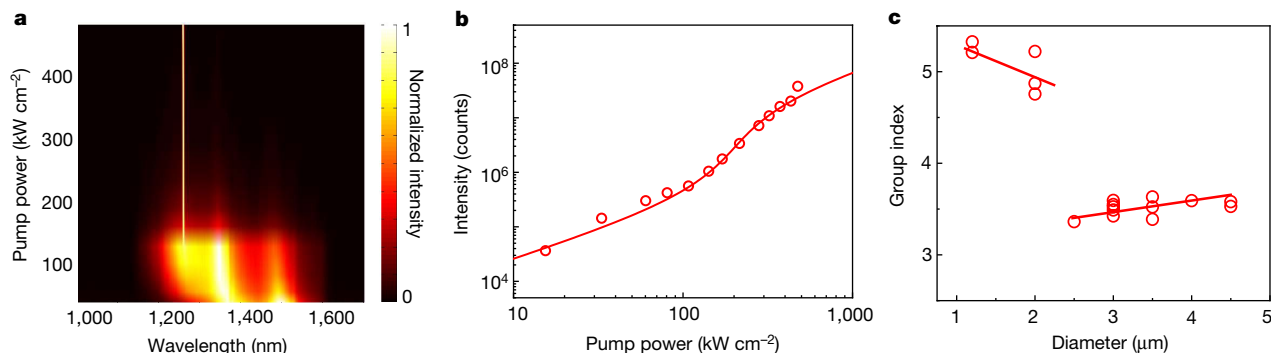

Fig. 4 | Lasing characteristics of sodium-based plasmonic nanolasers. a, Normalized spectra of the sodium-based plasmonic nanolaser at different pump powers. b, Light–light curve of the plasmonic nanolaser. The circle symbols represent experimental data and the line is a fit to the data. The substantially narrowed emission linewidth above the lasing threshold in a and the S-shaped light–light curve in b show a clear phase transition from spontaneous emission to lasing emission of the device. c, The group index versus device diameter estimated from the mode spacing in lasing spectra.

by systematic comparison with the reported devices based on noble metals. Furthermore, we show that these sodium-based plasmonic devices can operate stably over several months. Our results provide an alternative pathway to low-loss plasmonic materials. The convenient fabrication process and the state-of-the-art performance of the sodium-based plasmonic devices open up opportunities for advanced plasmonic applications.

Online content

Any methods, additional references, Nature Research reporting summaries, source data, extended data, supplementary information, acknowledgements, peer review information; details of author contributions and competing interests; and statements of data and code availability are available at https://doi.org/10.1038/s41586-020-2306-9.

1. Maier, S. A. *Plasmonics: Fundamentals and Applications* (Springer Science and Business Media, 2007).
2. Ozbay, E. Plasmonics: merging photonics and electronics at nanoscale dimensions. *Science* **311**, 189–193 (2006).
3. Gramotnev, D. K. & Bozhevolnyi, S. I. Plasmonics beyond the diffraction limit. *Nat. Photon*. **4**, 83–91 (2010).
4. Schuller, J. A. et al. Plasmonics for extreme light concentration and manipulation. *Nat. Mater*. **9**, 193–204 (2010).
5. Fang, Y. R. & Sun, M. T. Nanoplasmonic waveguides: towards applications in integrated nanophotonic circuits. *Light Sci. Appl*. **4**, 294 (2015).
6. Atwater, H. A. & Polman, A. Plasmonics for improved photovoltaic devices. *Nat. Mater*. **9**, 205–213 (2010).
7. Ma, R. M. & Oulton, R. F. Application of nanolasers. *Nat. Nanotechnol*. **14**, 12–22 (2019).
8. Valentine, J. et al. Three-dimensional optical metamaterial with a negative refractive index. *Nature* **455**, 376–379 (2008).
9. Gabrielli, L. H. et al. Silicon nanostructure cloak operating at optical frequencies. *Nat. Photon*. **3**, 461–463 (2009).
10. Lal, S., Link, S. & Halas, N. J. Nano-optics from sensing to waveguiding. *Nat. Photon*. **1**, 641–648 (2007).
11. Chung, T., Lee, S. Y., Song, E. Y., Chun, H. & Lee, B. Plasmonic nanostructures for nano-scale bio-sensing. *Sensors* **11**, 10907–10929 (2011).
12. Fang, N., Lee, H., Sun, C. & Zhang, X. Sub-diffraction-limited optical imaging with a silver superlens. *Science* **308**, 534–537 (2005).
13. Liu, Z. W., Lee, H., Xiong, Y., Sun, C. & Zhang, X. Far-field optica hyperlens magnifying sub-diffraction-limited object. *Science* **315**, 1686 (2007).
14. Boltasseva, A. & Atwater, H. A. Low-loss plasmonic metamaterials. *Science* **331**, 290–291 (2011).
15. Khurgin, J. B. How to deal with the loss in plasmonics and metamaterials. *Nat. Nanotechnol*. **10**, 2–6 (2015).
16. Naik, G. V., Shalaev, V. M. & Boltasseva, A. Alternative plasmonic materials: beyond gold and silver. *Adv. Mater*. **25**, 3264–3294 (2013).
17. Palik, E. D. *Handbook Of Optical Constants Of Solids* Vol. 3 (Academic Press, 1998).
18. Johnson, P. B. & Christy, R. W. Optical constants of the noble metals. *Phys. Rev. B* **6**, 4370–4379 (1972).
19. Smith, N. V. Optical constants of sodium and potassium from 0.5 to 4.0 eV by split-beam ellipsometry. *Phys. Rev.* **183**, 634–644 (1969).
20. Inagaki, T., Emerson, L. C., Arakawa, E. T. & Williams, M. W. Optical properties of solid Na and Li between 0.6 and 3.8 eV. *Phys. Rev. B* **13**, 2305–2313 (1976).
21. Ge, Y. C. Optical absorption study on the annealing behavior of metallic colloids in KCl:K crystals. *Spectrosc. Lett*. **31**, 123–134 (1998).
22. Chen, W., Thoreson, M. D., Ishii, S., Kildishev, A. V. & Shalaev, V. M. Ultra-thin ultra-smooth and low-loss silver films on a germanium wetting layer. *Opt. Express* **18**, 5124–5134 (2010).
23. Yang, H. U. et al. Optical dielectric function of silver. *Phys. Rev. B* **91**, 235137 (2015).
24. Mori, T. et al. Optical properties of low-loss Ag films and nanostructures on transparent substrates. *ACS Appl. Mater. Interf*. **10**, 8333–8340 (2018).
25. Ma, R. M. Lasing under ultralow pumping. *Nat. Mater*. **18**, 1152–1153 (2019).
26. Ning, C. Z. Semiconductor nanolasers and the size-energy-efficiency challenge: a review. *Adv. Photon*. **1**, 014002 (2019).
27. Wang, D., Wang, W., Knudson, M. P., Schatz, G. C. & Odom, T. W. Structural engineering in plasmon nanolasers. *Chem. Rev*. **118**, 2865–2881 (2018).
28. Gwo, S. & Shih, C. K. Semiconductor plasmonic nanolasers: current status and perspectives. *Rep. Prog. Phys*. **79**, 086501 (2016).
29. Hill, M. T. & Gather, M. C. Advanced in small lasers. *Nat. Photon*. **8**, 908–918 (2014).
30. Berini, P. & De Leon, I. Surface plasmon-polariton amplifiers and lasers. *Nat. Photon*. **6**, 16–24 (2012).
31. Ma, R. M., Oulton, R. F., Sorger, V. J., Bartal, G. & Zhang, X. Room temperature sub-diffraction-limited plasmon laser by total internal refection. *Nat. Mater*. **10**, 110–113 (2011).
32. Wang, S., Chen, H. Z. & Ma, R. M. High performance plasmonic nanolasers with external quantum efficiency exceed 10%. *Nano Lett*. **18**, 7942–7948 (2018).
33. Wang, S. et al. Unusual scaling laws for plasmonic nanolasers beyond the diffraction limit. *Nat. Commun*. **8**, 1889 (2017).

Article

Methods

Thermo-assisted spin-coating process of low-loss sodium film

Extended Data Fig. 1a shows the thermo-assisted spin-coating procedure for the sodium film. The sodium brick was melted to form a droplet on a tungsten boat when it was heated up to 160 °C in an inert-atmosphere-equipped glove box. The oxide shell on the surface of the droplet can be peeled off using tweezers. The liquid sodium can then be dropped onto a fast-spinning quartz substrate on a spin coater. The quartz substrate is ultrasmooth (root-mean-square surface roughness of about 0.1 nm), as shown in Extended Data Fig. 1b. The sodium–glass interface was then prepared. The sodium film, once packaged with epoxy, can be transferred freely out of the glove box.

Dielectric constant characterization

The dielectric constant ε of the sodium film was measured using an ellipsometer (RC2 UI, J. A. Woollam) ranging from 400 nm to 1,500 nm (see Extended Data Fig. 2a). The incident light through the silica substrate can be separated into two light spots; the detector receives only the light from the metal–silica interface. We use the Lorentz model (equations (3)–(5)) to fit the measured data. For the ultraviolet pole and the infrared pole, ε is expressed as

$$\varepsilon_{\text{pole},n} = C_n/(E_n^2 - E^2),\tag{3}$$

where C_n (in units of eV^2) and E_n (in units of eV) are fitting parameters, E is the photon energy (in units of eV) and n is the oscillator number. For the general Lorentz oscillator, ε is expressed as

$$\varepsilon_{\text{Lorentz},m} = A_m B_m E_m/(E_n^2 - E^2 - iEB_m).\tag{4}$$

Here A_m (unitless), B_m (in units of eV) and E_m (in units of eV) are the fitting parameters, where A_m approximately equals ε_2 at its peak value and B_m is approximately the full-width at half-maximum. m is the oscillator number. In the full wavelength range, the overall dielectric function is

$$\varepsilon(E) = \varepsilon_1(E) - i\varepsilon_2(E) = \varepsilon_{\text{offset}} + \varepsilon_{\text{pole},n} + \varepsilon_{\text{Lorentz},m},\tag{5}$$

where $\varepsilon_{\text{offset}}$ and $\varepsilon_{\text{pole},n}$ are real, and contribute only to ε_1. The oscillator functions are complex and therefore contribute to both ε_1 and ε_2.

Comparison of real and imaginary parts of dielectric functions of sodium and silver

Extended Data Fig. 2b, c shows a comparison of the dielectric functions of sodium and silver. Clearly, the optical loss (the imaginary part) of sodium is lower than that for silver, especially in the infrared region. We further compare the figure of merit ($-\varepsilon_1/\varepsilon_2$) in Extended Data Fig. 2d. The data for silver are measurements taken from the literature[17,18,23,24,34–37].

Fabrication of nanostructured sodium film

A thin Ag film (about 30 nm) was evaporated onto the quartz (thickness about 0.2 mm) as a conductive layer using physical vapour deposition (Gatan 682), and double hole arrays were made on the quartz substrate via focused-ion-beam milling (Dual-beam FIB 235, FEI Strata). After the focused-ion-beam process, the Ag film on the surface of the quartz was removed with HNO$_3$, followed by the thermo-assisted spin-coating process for the sodium film described above.

Measurement of propagation of SPP mode on sodium-quartz interface

The fabrication process for the plasmonic waveguide devices is shown in Extended Data Fig. 3. For effective coupling and decoupling of SPP along the sodium–quartz interface, the quartz substrate was first milled with a focused ion beam to generate periodic patterns at both coupling and out-coupling positions. The laser (Fianium SC-400-4 Compact) was concentrated onto the sodium nanostructures by an objective lens. Coupled-out signals was also captured by the objective lens. Finally, both input and output signals were collected with an infrared charge coupled device (XEVA-1083, Xenics) by a beam splitter. We measured several different propagation separations and fitted the intensity decay curve to unambiguously obtain the propagation lengths at different wavelengths on the sodium–quartz interface.

Comparison of sodium plasmonic waveguides with silver-based ones

We fabricated and measured the δ_{SPP} of both sodium and silver plasmonic waveguide as shown in Extended Data Fig. 4a–c. The sodium supports longer δ_{SPP} than silver in the wavelength range >1 μm. It should be noted that, besides δ_{SPP}, the effective mode size is another essential parameter of a plasmonic waveguide, characterizing the field-confinement capability. It is represented by the decay lengths (skin depths) in the dielectric δ_d and in the metal δ_m. Therefore, for evaluating the plasmonic waveguide, comparing δ_{SPP} alone is not comprehensive, and the figure of merit of the plasmonic waveguide ($\delta_{\text{SPP}}/(\delta_d + \delta_m)$) is usually used. In Fig. 2g we benchmarked our sodium plasmonic waveguide with the two silver-based references. To further clarify this point, we have calculated the figure of merit of the plasmonic waveguide for Ag plasmonic waveguides from the dielectric functions reported in a number of representative publications[17,18,23,24,34–37]. From Extended Data Fig. 4d, one can unambiguously come into the conclusion that our sodium-based plasmonic waveguide has state-of-the-art performance.

Detailed fabrication process for plasmonic nanolasers

The detailed fabrication process of the plasmonic nanolasers is shown in Extended Data Fig. 5. Electron-beam lithography and inductively coupled plasma etching were used to pattern InGaAsP MQWs nanodisks onto an epi-wafer (Extended Data Fig. 5a, b). 500-nm-thick SiO$_2$ was deposited on the nanodisks by chemical vapour deposition (Extended Data Fig. 5c). Then the whole sample was bonded onto quartz using a benzocyclobutene adhesive layer (Extended Data Fig. 5d), after which the InP substrate was removed by wet etching using HCl solution. Atomic layer deposition was used to deposit 7-nm-thick Al$_2$O$_3$ onto the nanodisk (Extended Data Fig. 5e). Finally, the sodium film was spin-coated onto nanodisks and the sample was packaged onto quartz by epoxy (Extended Data Fig. 5f).

Optical characterization of plasmonic nanolasers

Sodium-based plasmonic nanolasers were optically pumped by a nanosecond pump laser (1,064 nm, pulse length 5 ns, repetition rate 12 kHz), focused on the sample with an objective lens (50×, numerical aperture 0.42). The pump laser spot is about 7 μm in diameter. The emission from a nanolaser was collected by the same objective and guided to an InGaAs infrared camera and a near-infrared spectrometer. All experiments were carried out at room temperature.

Numerical simulation of the sodium-based plasmonic nanolaser

We carried out three-dimensional full-wave simulations via commercial software COMSOL multiphysics (radio-frequency module) to calculate the optical modes of the nanolasers. The Q factors of the cavity modes were evaluated as $Q = f_r/\delta f$, where f_r and δf represent the resonance frequency and the full-width at half-maximum of the resonance spectrum, respectively.

Comparison of sodium-based plasmonic nanolasers with noble-metal-based ones

Extended Data Table 1 shows a comparison of sodium-based plasmonic nanolasers with reported noble-metal-based ones operated in the near-infrared range[38–49]. In the table, the feedback mechanism, physical size, gain medium, emission wavelength, pump condition, working temperature and lasing threshold in peak power density are

listed for comparison. Extended Data Fig. 8 shows the lasing thresholds and physical volumes of reported room-temperature plasmonic nanolasers in the near-infrared range.

Data availability

We declare that the data supporting the findings of this study are available within the paper.

34. McPeak, K. M. et al. Plasmonic films can easily be better: rules and recipes. *ACS Photon*. **2**, 326–333 (2015).
35. Babar, S. & Weaver, J. H. Optical constants of Cu, Ag, and Au revisited. *Appl. Opt.* **54**, 477–481 (2015).
36. Werner, W. S. M., Glantschnig, K. & Ambrosch-Draxl, C. Optical constants and inelastic electron-scattering data for 17 elemental metals. *J. Phys. Chem. Ref. Data* **38**, 1013–1092 (2009).
37. Ciesielski, A., Skowronski, L., Trzinski, M. & Szoplik, T. Controlling the optical parameters of self-assembled silver films with wetting layers and annealing. *Appl. Surf. Sci.* **421B**, 349–356 (2017).
38. Hill, M. T. et al. Lasing in metal–insulator–metal sub-wavelength plasmonic waveguides. *Opt. Express* **17**, 11107–11112 (2009).
39. Khajavikhan, M. et al. Thresholdless nanoscale coaxial lasers. *Nature* **482**, 204–207 (2012).
40. Zhou, W. et al. Lasing action in strongly coupled plasmonic nanocavity arrays. *Nat. Nanotechnol.* **8**, 506–511 (2013).
41. Yang, A. et al. Real-time tunable lasing from plasmonic nanocavity arrays. *Nat. Commun.* **6**, 6939 (2015).
42. Keshmarzi, E. K., Tait, R. N. & Berini, P. Single-mode surface plasmon distributed feedback lasers. *Nanoscale* **10**, 5914–5922 (2018).
43. Kwon, S.-H. et al. Subwavelength plasmonic lasing from a semiconductor nanodisk with silver nanopan cavity. *Nano Lett.* **10**, 3679–3683 (2010).
44. Marell, M. J. H. et al. Plasmonic distributed feedback lasers at telecommunications wavelengths. *Opt. Express* **19**, 15109–15118 (2011).
45. Kwon, S.-H. et al. Surface plasmonic nanodisk/nanopan lasers. *IEEE J. Quantum Electron.* **47**, 1346–1353 (2011).
46. Lakhani, A. M. et al. Plasmonic crystal defect nanolaser. *Opt. Express* **19**, 18237–18245 (2011).
47. Ho, J. et al. Low-threshold near-infrared GaAs-AlGaAs core-shell nanowire plasmon laser. *ACS Photon.* **2**, 165–171 (2015).
48. Ho, J. et al. A nanowire-based plasmonic quantum dot laser. *Nano Lett.* **16**, 2845–2850 (2016).
49. Lee, C.-J. et al. Low-threshold plasmonic lasers on a single-crystalline epitaxial silver platform at telecom wavelength. *ACS Photon.* **4**, 1431–1439 (2017).

Author contributions J.Z., R.-M.M. and S.Z. conceived and supervised the project. Y.W., J.Y., Y.-F.M. and X.C. fabricated the samples. J.Y. collected dielectric function data. Y.W., J.Y., J.C. and T.L. acquired the surface plasma propagation data. S.W., S.-Y.W. and Y.-F.M. collected and analysed lasing data. H.-Z.C. performed the lasing mode simulations. Y.Z. and L.Z. calculated the plasmon damping rate. Y.W., J.Y., S.W., J.Z., R.-M.M. and W.C. wrote the paper with input from all authors.

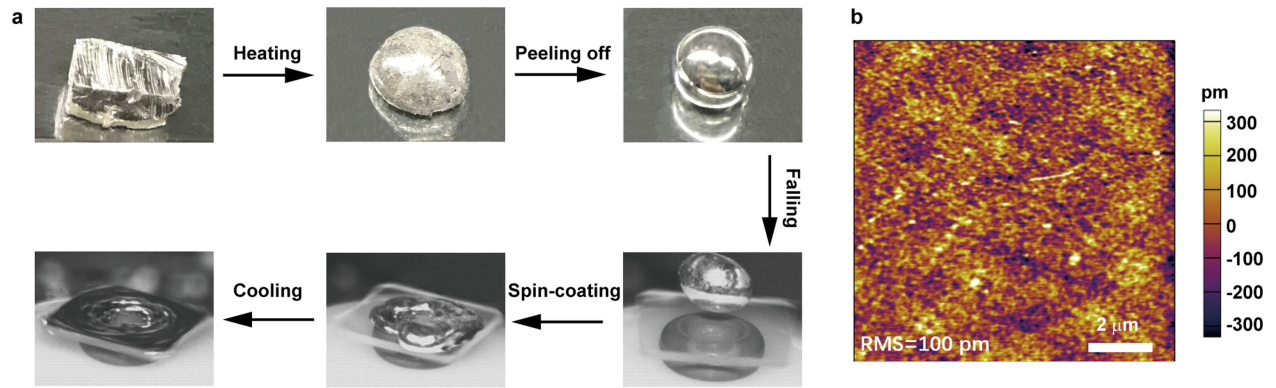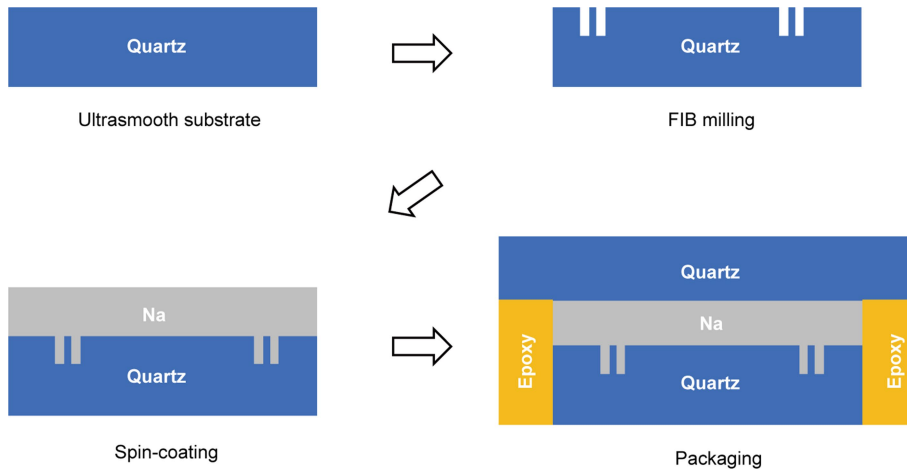**Competing interests** The authors declare no competing interests.

Extended Data Fig. 1 | The thermo-assisted spin-coating procedure for the low-loss sodium film. a, Optical images of the procedure. **b**, Atomic force microscope topology of the smooth quartz surface, which shows that the root mean square (RMS) roughness is about 100 pm.
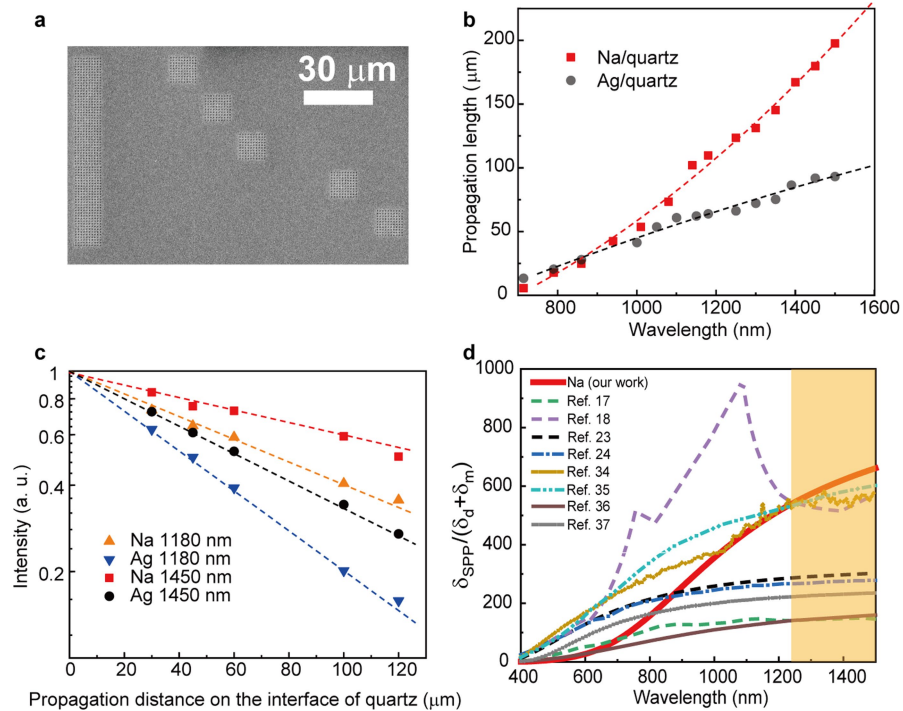
Extended Data Fig. 2 | Dielectric function measurements for sodium and comparison with silver. a, Schematic of ellipsometer measurements. The incident light transmits through the upper surface to the lower surface of the silica layer (contact with the sodium interface) and reflects back. The light reflected from the sodium/glass interface can be detected. **b**, Comparison of real (**a**) and imaginary (**b**) parts as well as the figure of merit ($-\varepsilon_1/\varepsilon_2$) (**c**) of the dielectric functions of silver and sodium (this work). The data for silver are taken from the literature[17,18,23,24,34–37].
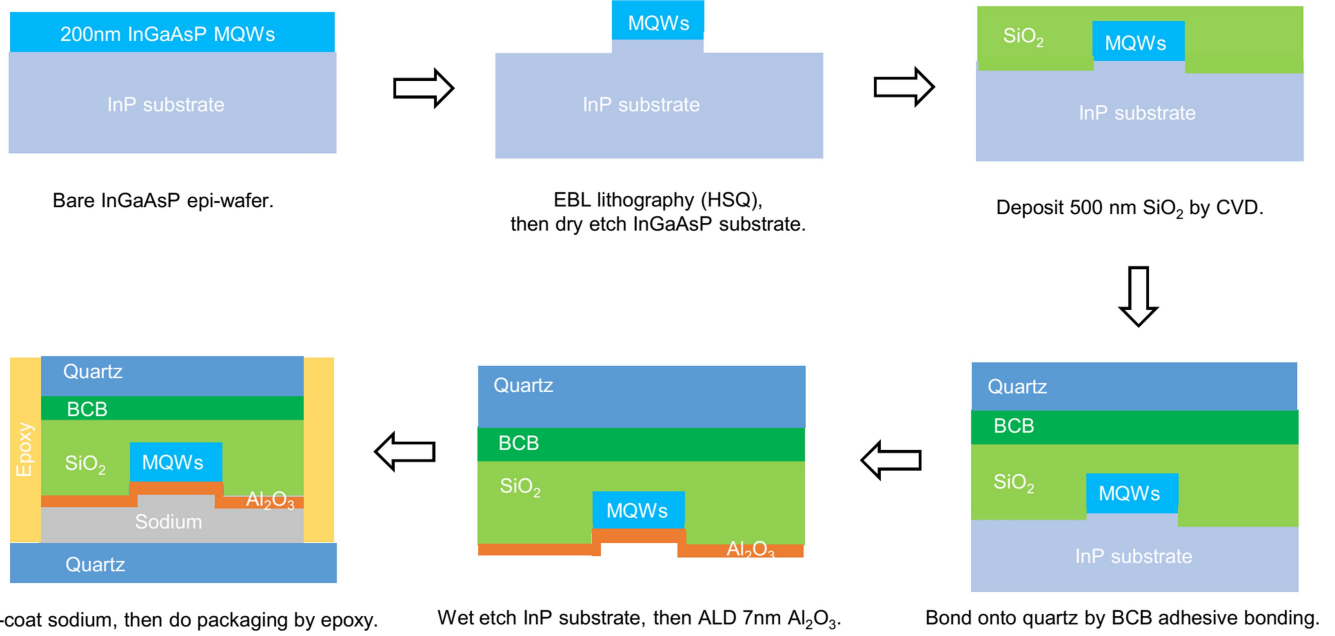
Extended Data Fig. 3 | Detailed fabrication process of the plasmonic waveguides. FIB, focused ion beam.
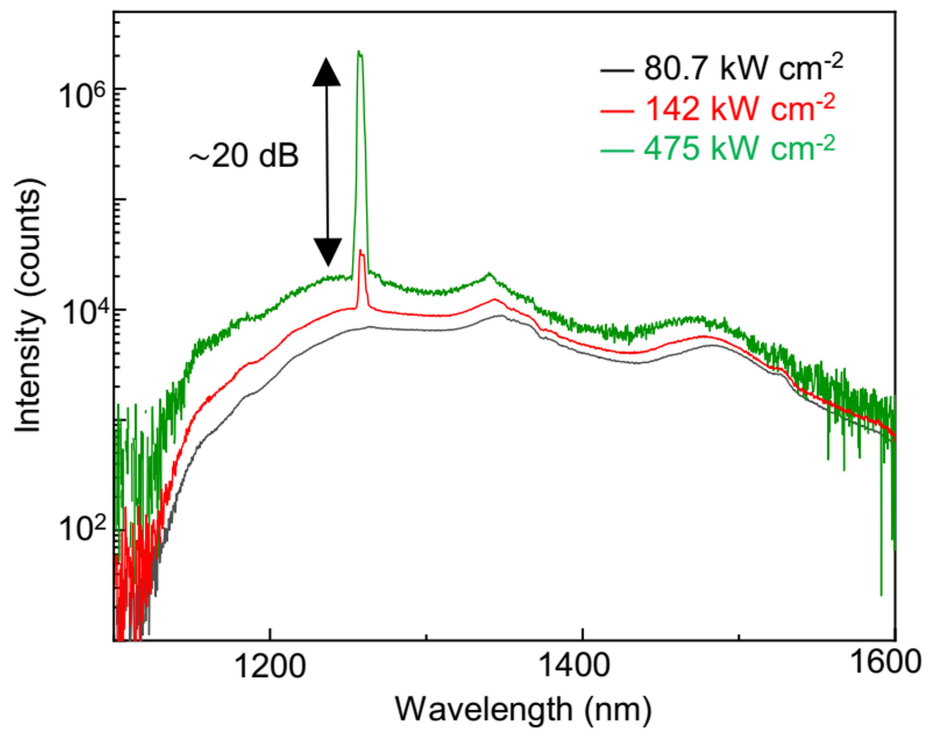
a

30 μm

b

c

d

Extended Data Fig. 4 | Comparison of silver and sodium plasmonic waveguides. a, SEM image of the launching and outcoupling structures of plasmonic waveguides. **b**, The fitted δ_{SPP} at different wavelengths on the quartz interface. The dashed line is a fit to the data. **c**, Propagation measurements at wavelengths of 1,180 nm and 1,450 nm for sodium and silver, with the exponential curves fitted to the data. **d**, F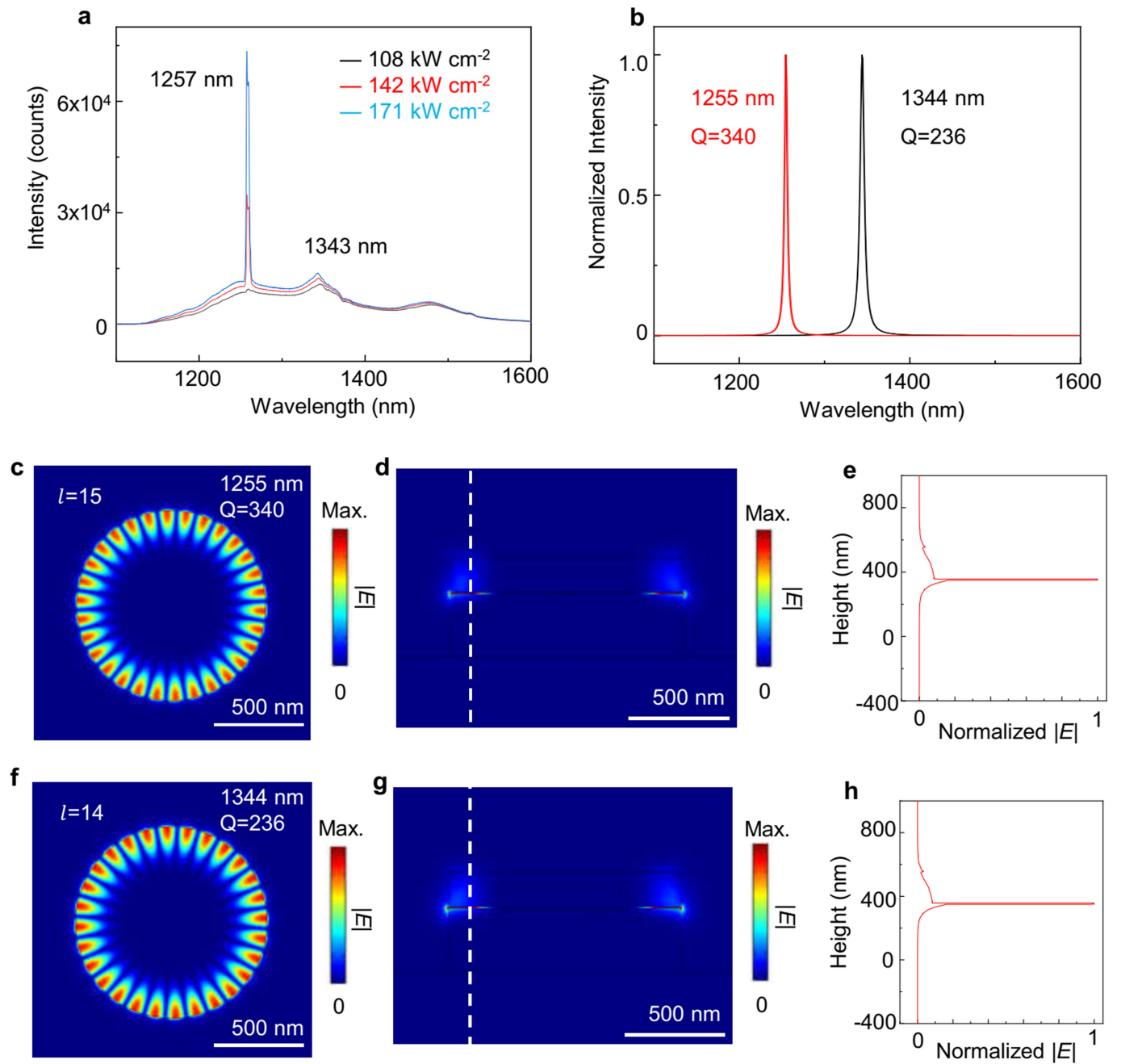igures of merit for sodium to silver plasmonic waveguides. The figure of merit of the plasmonic waveguides is defined as the ratio of propagation length to skin depth $\delta_{SPP}/(\delta_d + \delta_m)$. The sodium data are calculated from the measured dielectric function, and the silver data are calculated using the dielectric function, taken from a number of representative publications[17,18,23,24,34–37].

Article

Extended Data Fig. 5 | Detailed fabrication process of the sodium-based plasmonic nanolaser. BCB, benzocyclobutene; HSQ, hydrogen silsesquioxane; EBL, electron-beam lithography; ALD, atomic layer deposition; CVD, chemical vapour deposition.
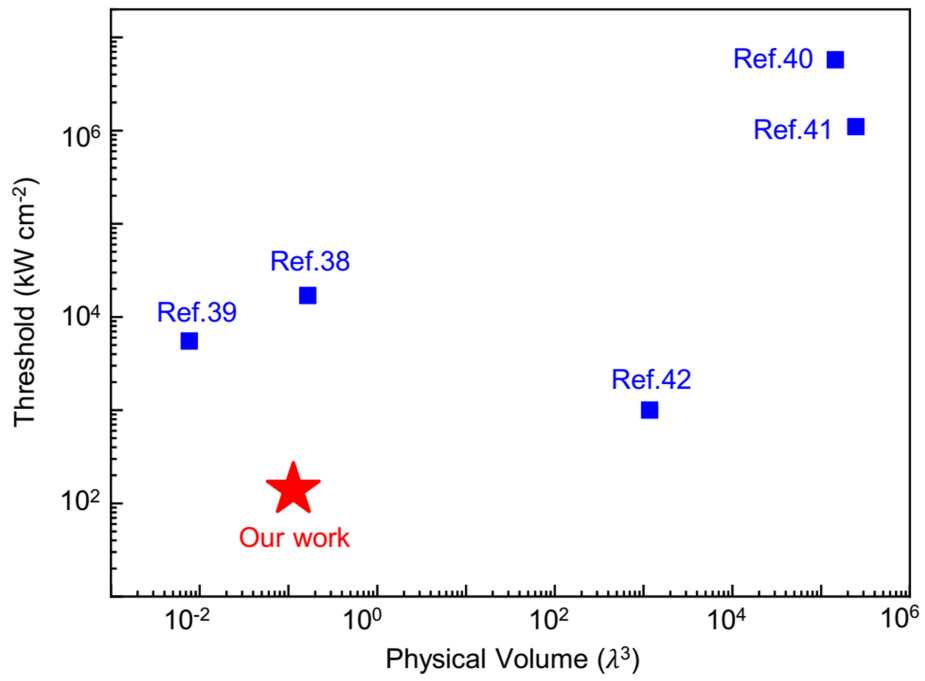
Extended Data Fig. 6 | Emission spectra (semi-logarithmic scale) of the plasmonic nanolaser shown in the main text for different pump powers. When the pump intensity is 475 kW cm^{-2}, the device shows single-mode lasing with a side-mode suppression ratio of 20 dB.
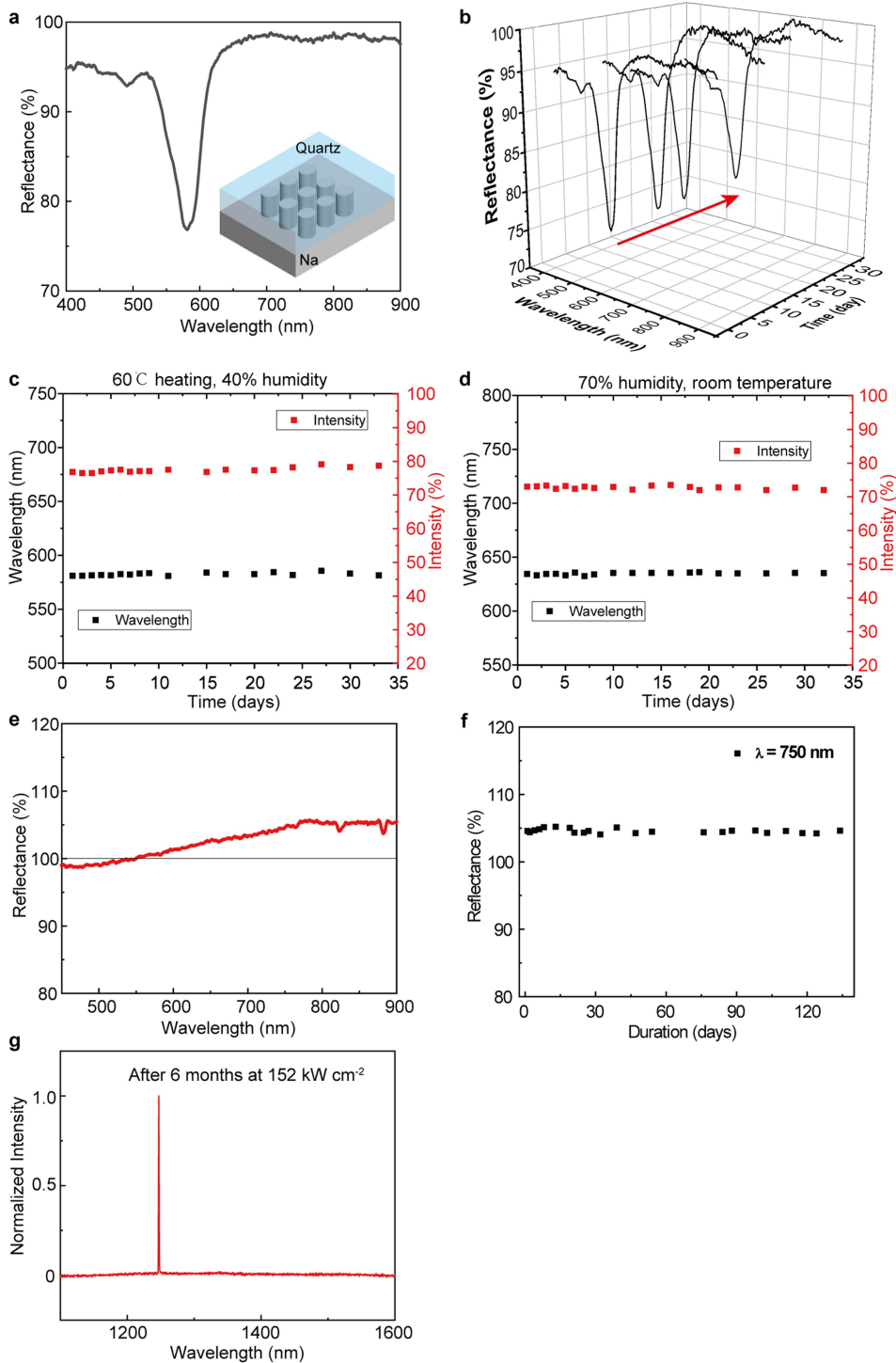
Extended Data Fig. 7 | Numerical simulation of the cavity modes of the sodium-based plasmonic nanolaser. a, Measured emission spectra of the plasmonic nanolaser around the lasing threshold, which exhibit two clear cavity modes at wavelengths of 1,257 nm and 1,343 nm respectively. **b**, Spectrum profile of the two cavity modes, where the resonant wavelength and the linewidth are obtained from the simulation. We assumed Lorentz-shape spectrum profiles here. The simulation shows that the cavity modes at wavelengths of 1,257 nm and 1,343 nm can be identified as plasmonic

whispering-galley modes with azimuthal orders of 15 and 14, respectively, and the corresponding quality factors Q of these two modes are 340 and 236, respectively. **c**, **d**, Top (**c**) and side (**d**) views of simulated electric-field distributions of the plasmonic whispering-galley modes with azimuthal order of 15. **e**, Electric-field profile E extracted from the white dashed line in **d**. **f**, **g**, Top (**f**) and side (**g**) views of simulated electric-field distributions of the plasmonic whispering-galley modes with azimuthal order of 14. **h**, Electric-field profile extracted from the white dashed line in **g**.

Extended Data Fig. 8 | Comparison of our work to reported plasmonic lasers in terms of the threshold and cavity size. Blue square symbols represent reported plasmonic nanolasers in the literature. The red star represents our sodium-based plasmonic nanolaser. λ is the lasing emission wavelength in free space.

Extended Data Fig. 9 | Stability test for sodium-based reflective plasmonic filters, sodium mirror and plasmonic nanolasers. a–d, Accelerated ageing tests for sodium-based reflective plasmonic filters. **a**, Reflectance spectrum of a representative filter device. Inset, schematic of the device. **b**, Reflectance spectra over time. **c**, Stability of a fabricated device in terms of the resonance wavelength and intensity at 60 °C, with air humidity 40%. **d**, Stability of a fabricated device in terms of the resonance wavelength and intensity at room temperature and air humidity 70%. **e**, **f**, Stability of the sodium mirror. **e**, Reflectance spectrum of the sodium mirror against a standard silver mirror (Thorlabs, PF10-03-P01). **f**, Reflectance of the packaged sodium mirror at wavelength $\lambda = 750$ nm over 120 days in air. **g**, Lasing spectrum of a sodium-based plasmonic nanolaser after six months.

Extended Data Table 1 | Performance comparison of near-infrared plasmonic nanolasers

Table 1|Performance comparison of near-infrared plasmonic nanolasers

Year	Type	Feedback	Size	Gain medium	Emission Wavelength	Pump	Temperature	Threshold	Refs
2020	Plasmonic nanodisk	WGM	Diameter: 1.2 μm Height: 200 nm	InGaAsP	1257 nm	Optical, pulsed	Room Temperature	140 kW cm^{-2}	Our work
2009	Gap plasmon	FP	Thickness: 310 nm Length: 6 μm	InGaAs	1500 nm	Electrical, continuous wave	Room Temperature	17 MW cm^{-2}	38
2012	Plasmonic coaxial	FP	Diameter: 500 nm Height: 260 nm	InGaAsP	1400 nm	Optical, continuous wave /pulsed	Room Temperature	5.5 MW cm^{-2}	39
2013	Plasmonic nanocavity array	Bandedge lattice plasmons	Diameter: 130 nm Period: 600 nm Height: 60 nm	Dye	913 nm	Optical, pulsed	Room temperature	5.75 GW cm^{-2}	40
2015	Plasmonic nanocavity array	Bandedge lattice plasmons	Diameter: 120 nm Period: 600 nm Depth: 150 nm	Dye	855 nm	Optical, pulsed	Room temperature	1.1 GW cm^{-2}	41
2018	Plasmonic DFB	FP	Length: 2 mm Width: 1 μm Height: 450 nm	Dye	800 nm	Optical, pulsed	Room Temperature	1 MW cm^{-2}	42
2010	Plasmonic nanodisk	WGM	Thickness: 235 nm Diameter: 1 μm	InAsP	1300 nm	Optical, pulsed	8 K	120 kW cm^{-2}	43
2011	Plasmonic DFB	FP	Width: 140 nm Length: 4 μm	InGaAs	1550 nm	Electrical, continuous wave	80 K	134 kW cm^{-2}	44
2011	Plasmonic nanodisk	WGM	Diameter: 1.25 μm Height: 235 nm	InP	1300 nm	Optical, pulsed	8 K	26 kW cm^{-2}	45
2011	Plasmonic crystal defect	FP	Width: 380 nm Length: 14 μm	InGaAsP	1350 nm	Optical, pulsed	77 K	100 kW cm^{-2}	46
2015	Plasmonic nanowire	FP	Diameter: 150 nm Length: 4.77 μm	AlGaAs/GaAs	800 nm	Optical, pulsed	8 K	4 MW cm^{-2}	47
2016	Plasmonic nanowire	FP	Diameter: 180 nm Length: 2.3 μm	GaAs	850 nm	Optical, pulsed	7 K	2.4 MW cm^{-2}	48
2017	Plasmonic nanowire	FP	Length: 4.8 μm Width: 380 nm Height: 140 nm	InGaAsP	1300 nm	Optical, continuous wave	125 K	1.4 MW cm^{-2}	49

DFB, distributed feedback; WGM, whispering gallery mode; FP, Fabry-Perot.